

Surface states and local spin susceptibility in doped three-dimensional topological insulators with odd-parity superconducting pairing symmetry

Björn Zocher^{1,2} and Bernd Rosenow¹

¹*Institut für Theoretische Physik, Universität Leipzig, D-04103 Leipzig, Germany*

²*Max Planck Institut für Mathematik in den Naturwissenschaften, D-04103 Leipzig, Germany*

(Dated: October 19, 2012)

We investigate characteristic features in the spin response of doped three-dimensional topological insulators with odd-parity unequal-spin superconducting pairing, which are predicted to have gapless Majorana surface modes. These Majorana modes contribute to the local spin susceptibility, giving rise to a characteristic temperature behavior of the Knight shift and the spin-lattice relaxation time in magnetic resonance experiments. Because of their different decay lengths, the Majorana modes can be observed and clearly distinguished from the Dirac modes of the topological insulator by local probes which allow for a depth-controlled study of the electron spins on the nanometer length scale.

PACS numbers: 73.20.At, 74.20.Rp, 74.25.Ha, 74.25.nj

Topological insulators (TIs) are time-reversal invariant systems with gapped bulk and protected massless Dirac modes at the surface [1, 2]. Very soon after the discovery of TIs, theorists generalized this concept to topological superconductors (TSCs) which are characterized by a superconducting (SC) gap in the bulk and protected gapless Majorana surface modes [1–6]. Semiconductors like the bismuth chalcogenides with strong spin-orbit coupling and a Fermi surface centered at the time-reversal-invariant momentum, are of particular interest because of their single helical Dirac cone at the surface [7]. Copper doped Bi_2Se_3 is an unconventional SC [8–11] with non-trivial surface states and a band structure similar to that of Bi_2Se_3 but with shifted chemical potential, reduced Fermi velocity, and enlarged surface dispersion [9].

By now, the surface states in $\text{Cu}_x\text{Bi}_2\text{Se}_3$ have been probed by photoemission [9] and point contact spectroscopy [12, 13]. Nuclear magnetic resonance (NMR) and quadrupole resonance, as well as the electron (ESR) and muon spin resonance (μSR) are another class of powerful techniques to investigate the electronic properties locally. These probes measure the spin susceptibility which is directly connected to the spin structure of the SC pairing. In this letter, we study characteristic features in the spin response of odd-parity pairing in doped TIs and predict clear signatures for the above resonance techniques.

Fu and Berg [14] showed that strong spin-orbit coupled bands indeed favor an odd-parity interorbital unequal-spin pairing [15, 16]. To gain insight into its topological non-trivial nature, we map this pairing Hamiltonian onto the conduction band which yields an effective time-reversal invariant $p \pm ip$ pairing in three dimensions. Because of this topology, there is a pair of Majorana zero-energy modes (MZM) located at each surface and protected by time-reversal symmetry. Additionally there are unconventional Surface Andreev bound states (SABS) originating from the band inversion as shown in Ref. [17] for a linear $k \cdot p$ model. In addition to the linear

momenta, we here consider quadratic momentum terms which determine the energy range of coexistence between Dirac modes and unconventional SABS, and which may give rise to another species of zero-energy SABS. The main motivation for introducing the quadratic terms is the possibility to study the competition between the different surface states and the bulk. The coexistence of the MZMs and the SABS originating from the band inversion gives rise to two characteristic length scales. The Dirac modes decay on the nm scale ξ_0 whereas the decay length ξ_1 for the MZMs is hundreds of nm. Hence, the local spin susceptibility shows different characteristic behavior in the bulk, at the surface, and within ξ_1 into the bulk despite the spinless nature of the MZM. Conventional bulk NMR can distinguish between competing pairing symmetries by the characteristic temperature dependence of the Knight shift and the spin-lattice relaxation rate. We propose that depth controlled probes [18, 19] allow to clearly determine the pairing symmetry and investigate the MZMs. Our work is motivated by $\text{Cu}_x\text{Bi}_2\text{Se}_3$, however, our results are more generally relevant for other inversion symmetric materials such as the ternary chalcogenides [20] and the PbTe class [21, 22]. Furthermore, our findings for doped TIs are complementary to the superfluid $^3\text{He-B}$ phase [23, 24] where spin relaxation reflects the gapless Majorana nature.

In the following, we consider doped three-dimensional TIs described by the low-energy $k \cdot p$ Hamiltonian $H_{TI} = \sum_{\mathbf{k}} C_{\mathbf{k}}^\dagger \mathcal{H}_{TI}(\mathbf{k}) C_{\mathbf{k}}$ [7, 14], where

$$\mathcal{H}_{TI}(\mathbf{k}) = m_0(\mathbf{k})\sigma_x + v_z k_z \sigma_y + v(k_x s_y - k_y s_x)\sigma_z - \mu \quad (1)$$

with $m_0(\mathbf{k}) = m + B_1 k_z^2 + B_2(k_x^2 + k_y^2)$, $C_{\mathbf{k}} = (c_{i\mathbf{k}s})_{i,s}$, $B_1, v_z > 0$, and $m < 0$. Here, the s_i (σ_i) denote the Pauli matrices for the spin (orbital) degree of freedom, and the operators $c_{i\mathbf{k}s}$ annihilate an electron in orbital i , with momentum \mathbf{k} , and spin s . The unitary operator $\exp(i\phi s_z/2)$, where ϕ is the azimuthal angle (k_x, k_y) , transforms Hamiltonian Eq. (1) onto $\mathcal{H}_{TI}(k_x, 0, k_z)$ which reflects the rotational symmetry

around the z -axis. The doped charge density determines the chemical potential μ , and the Fermi surface is given by the equation $\mu^2 = m_0^2(\mathbf{k}_F) + v_z^2 k_{F,z}^2 + v^2(k_{F,x}^2 + k_{F,y}^2)$.

Possible pairing terms depend on the specific mechanism and the lattice symmetry. For pairing induced by on-site density-density interactions, Fu and Berg [14] showed that the spin-orbit coupled bands favor odd-parity interorbital unequal-spin pairing,

$$H_{SC} = \Delta \sum_{\mathbf{k}} \left(c_{1\uparrow} c_{2-\mathbf{k}\downarrow} + c_{1\downarrow} c_{2-\mathbf{k}\uparrow} \right) + h.c. \quad (2)$$

Here, the parity operator \mathcal{P} transforms $c_{1\mathbf{k}s}$ into $c_{2-\mathbf{k}s}$ and vice versa which yields $\mathcal{P}H_{SC}\mathcal{P}^{-1} = -H_{SC}$. If the pairing is induced by long-range interactions, such as the electron-phonon interaction, other unequal-spin pairing channels are also possible [15, 25]. Additionally, we consider (i) even-parity, intraorbital $\Delta_1(c_{1\uparrow}c_{1\downarrow} + c_{2\uparrow}c_{2\downarrow})$, (ii) odd-parity, intraorbital $\Delta_2(c_{1\uparrow}c_{1\downarrow} - c_{2\uparrow}c_{2\downarrow})$, and (iii) even-parity, interorbital $\Delta_3(c_{1\uparrow}c_{2\downarrow} - c_{1\downarrow}c_{2\uparrow})$ pairing.

To study the effect of spin-orbit coupling on the pairing symmetry, we project Eq. (2) onto the basis $(\alpha_{\mathbf{k},\tau})$ spanned by the conduction band of the bulk TI Eq. (1). This yields the effective pairing Hamiltonian

$$H_{SC} \approx i\Delta \sum_{\mathbf{k}} \frac{v_z k_z + ivk \frac{m_0(\mathbf{k})}{\mu}}{E_0(\mathbf{k})} \alpha_{\mathbf{k},+} \alpha_{-\mathbf{k},-} + h.c. \quad (3)$$

where $E_0^2(\mathbf{k}) = v_z^2 k_z^2 + v^2 k^2$ and $k^2 = k_x^2 + k_y^2$. The effective pairing Hamiltonian is exact in first order in Δ/μ and yields a gapped bulk excitation spectrum with quasiparticle gap $2\Delta E_0(\mathbf{k})/\mu$. The operators $\alpha_{\mathbf{k},\tau}$ and $\alpha_{-\mathbf{k},\tau}$ transform into each other under time-reversal while $\mathcal{P}\alpha_{\mathbf{k},\tau}\mathcal{P}^{-1} = \tau\alpha_{-\mathbf{k},-\tau}$ [25]. The corresponding Bogoliubov-de Gennes equations are in the same universality class as the ones for two copies of spinless SCs with opposite chirality, which is known to be a time-reversal invariant TSC with MZMs if the chemical potential lies within the conduction band [4, 26]. From this analogy, we expect to find a pair of MZMs for $k = 0$ and additionally a pair of zero-energy SABS whenever $m_0(\mathbf{k}_F) = 0$.

The Hamiltonian Eq. (1) confined in z -direction has a two-dimensional helical massless Dirac cone at the surface [7]. In contrast, we also know that the effective pairing Hamiltonian Eq. (3) yields a pair of helical MZMs at the time-reversal invariant momentum $k = 0$ [4]. Hence, we obtain two species of SABSs originating from the band inversion and the $p \pm ip$ pairing, respectively. We find these states by replacing $k_z \rightarrow -i\partial_z$ and solving the corresponding Schrödinger equation with boundary condition $\sigma_3\psi(z=0) = \psi(z=0)$. For the normal conducting Hamiltonian Eq. (1), we obtain the dispersion $E_{D,\tau}(k) = vk$ and the surface wave functions

$$\psi_{D,\tau}(z, k, \phi) = \sqrt{\nu/v_z} (e^{\nu z/v_z}, 0)_\sigma \otimes (1, i\tau e^{i\phi})_s, \quad (4)$$

where $\nu = (1 - \sqrt{1 + 4B_1(m + B_2 k^2)/v_z^2})/2B_1$. From this expression, we find the decay length $\xi_0 = 2B_1/v_z$

for $k^2 < (-m - v_z^2/4B_1)/B_2$ and $\xi_0 = 2B_1/v_z/(1 - \sqrt{1 + 4B_1(m + B_2 k^2)/v_z^2})$ for $(-m - v_z^2/4B_1)/B_2 < k^2 < -m/B_2$. For $k^2 \rightarrow -m/B_2$, ξ_0 diverges and the surface states become bulk states as shown in Fig. 1(a).

Similarly as for the Dirac modes, we find the $k = 0$ MZMs by solving the Schrödinger equation. Thus, we obtain the Majorana dispersion $E_M(k) \approx kv\Delta(m + B_1 k_{F,z}^2)/\mu^2$ near $k = 0$. The MZMs decay on a characteristic length ξ_1 as shown in Fig. 1(b) where we plot ξ_1 as function of the chemical potential. For $\mu > |m|$, we find $\xi_1(\mu) = v_{F,z}/\Delta$ with the Fermi velocity in z -direction $v_{F,z}$. Typical values for ξ_1 are by a factor of $E_0/\Delta \sim 10^2$ larger than ξ_0 . In contrast to the Dirac modes, the $k = 0$ MZMs exist for all values of the chemical potential and enter the bulk for $\mu \rightarrow \infty$ only. For both species of SABSs, the quadratic terms B_1 and B_2 significantly determine the behavior of the decay lengths. For $B_1 = B_2 = 0$, we obtain $\xi_0 = v_z/|m|$ and $\xi_1 = v_z/\Delta$ whereas the decay lengths for $B_1, B_2 > 0$ strongly depend on the Fermi velocity and thus on μ .

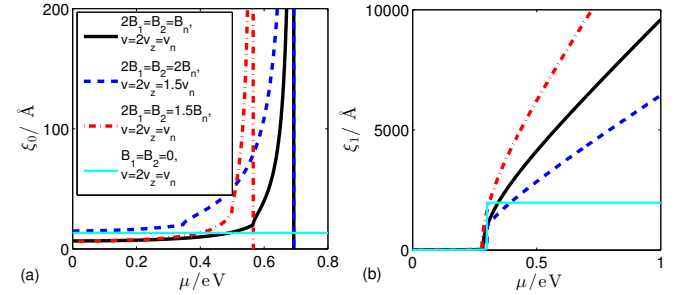


FIG. 1. (Color online) Decay lengths of (a) the Dirac mode of the TI and (b) the $k = 0$ MZM of the odd-parity interorbital SC with $\Delta = 1$ meV, $m = -0.3$ eV, $v_n = 4$ eV\AA, and $B_n = 10$ eV\AA². The lines are defined in panel (a).

Depending on the doped charge density, the SC state could occur with the chemical potential either in the region where the Dirac surface states are separated from the bulk conduction band [9] or where only the bulk states remain. Since the numerator of Eq. (3) vanishes for the Dirac modes with $k_z \rightarrow -iv/v_z$ and $\mu = vk$, they are not gapped by H_{SC} and yield a ring structure of zero-energy SABSs. Higher order terms which couple valence and conduction band do not change the character of the surface modes qualitatively. The authors of ref. [17] showed that a branch of SABSs connects the MZM and the Dirac-like SABS due to the mirror helicity of the Hamiltonian which here shows up as the sign of the mass $m_0(\mathbf{k}_F)$. This mass is negative near the bottom of the conduction band and changes sign for $\mu^2 = -mv_z^2/B_1, -mv^2/B_2$. For small chemical potentials, $\mu^2 < -mv_z^2/B_1, -mv^2/B_2$, the mass term is negative, and hence, both the MZM and the branch of zero-energy SABS originating from the Dirac mode exist. On the other hand, for large chemical potentials,

$-mv_z^2/B_1, -mv_z^2/B_2 < \mu^2$, the mass term $m_0(\mathbf{k}_F)$ is positive and only the $k = 0$ MZM exists. In the regime of intermediate μ , we distinguish two cases. For $-mv_z^2/B_1 \leq \mu^2 < -mv_z^2/B_2$, there is a momentum \mathbf{k}_F such that the mass term $m_0(\mathbf{k}_F)$ vanishes. This yields another species of zero-energy SABS emerging at $k = 0$ which now carries the negative velocity from the band inversion as expected from Eq. (3) and moves towards the Dirac mode with increasing μ . Then, both finite momentum SABS meet and gap out for $\mu^2 \rightarrow -mv_z^2/B_2$. In contrast, for $-mv_z^2/B_2 < \mu^2 < -mv_z^2/B_1$, the Dirac SABS disappeared in the bulk and is replaced by the unconventional SABS discussed by Hsieh and Fu [17] while $m + B_1 k_{F,z}^2$ is negative [25]. Moreover, with increasing chemical potential, this finite- k zero-energy SABS moves towards $k = 0$ and disappears for $\mu^2 \rightarrow -mv_z^2/B_1$. Thus, we conclude that the number of species of zero-energy SABS is even for $m^2 < \mu^2 < -mv_z^2/B_1$ and odd for $\mu^2 > -mv_z^2/B_1$. Hsieh and Fu [17] do not find the competition between these different sectors since the parameters B_1 and B_2 in their lattice model are small and thus they only consider the small chemical potential regime with the $k = 0$ MZM and one species of finite k modes.

In the following, we investigate signatures of the unconventional SABS in the local quasiparticle density of states (LDOS) and the local spin response of the TSC confined in z -direction. For the numerics we discretize the z -direction of Hamiltonian Eq. (1) with surfaces at $z = 0$ and $z = Na$ by replacing $k_z \psi \rightarrow -i(\psi_{n+1} - \psi_{n-1})/2a$ and $k_z^2 \psi \rightarrow -(\psi_{n+1} + \psi_{n-1} - 2\psi_n)/a^2$ where $z = na$. Motivated by the Bi chalcogenides [2], we use the parameters $N = 400$, $a = 6 \text{ \AA}$, $m = -0.3 \text{ eV}$, $v = 2v_z = 4 \text{ eV \AA}$, $B_2 = 2B_1 = 10 \text{ eV \AA}^2$, $\mu = 0.5 \text{ eV}$, and $\Delta = 3 \text{ meV}$. Here, B_2 is reduced as compared to Bi_2Se_3 [2] to guarantee the existence of the Dirac modes and its separation from the conduction band as found for $\text{Cu}_x\text{Bi}_2\text{Se}_3$ [9]. From the above analysis we know that the $k = 0$ MZMs and one finite k zero-energy SABS coexist in this regime. For abbreviation, we neglect the quadratic momentum terms in our analytical results where they mainly renormalize the Fermi velocity.

In figure 2(a) we plot the LDOS which shows two qualitatively distinct regions. In the bulk we obtain $\mathcal{N}_B(\epsilon) = 2\mu E_0(k_F)\epsilon/(\pi v^2 v_z \sqrt{\epsilon^2 - \Delta^2 E_0^2(k_F)/\mu^2})$ with quasiparticle gap $2\Delta E_0(k_F)/\mu$ and sharp coherence peak, while there is a finite midgap LDOS at the surface. Depending on whether the Dirac modes already crossed the bulk band, we distinguish between $\mu^2 > v^2|m|/B_2$ where only the MZMs appear with

$$\mathcal{N}_S(\epsilon, z \geq 0) \approx \epsilon \frac{\mu^4 e^{-2z/\xi_1}}{\pi \xi_1 v^2 m^2 \Delta^2} \sin^2\left(\frac{z E_0}{v_z}\right) \quad (5)$$

and $\mu^2 < v^2|m|/B_2$ where both MZM and Dirac-like SABS exist with

$$\mathcal{N}_S(\epsilon, z \geq 0) \approx \frac{\mu e^{-2z/\xi_0}}{\pi \xi_0 v^2} + \frac{\epsilon \mu^4 e^{-2z/\xi_1}}{\pi \xi_1 v^2 m^2 \Delta^2} \sin^2\left(\frac{z E_0}{v_z}\right) \quad (6)$$

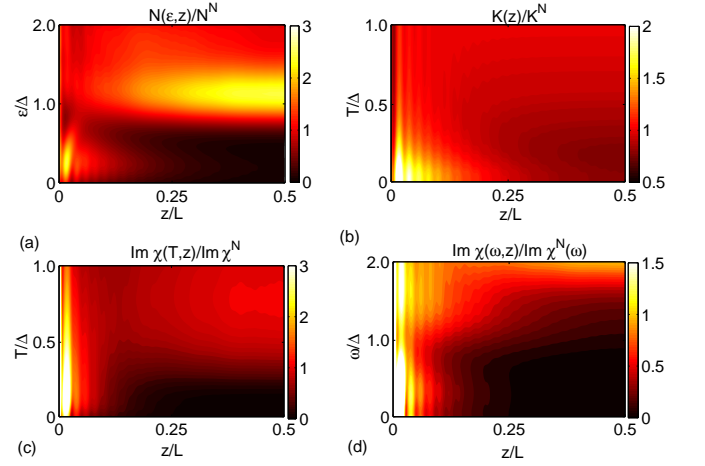


FIG. 2. (Color online) (a) LDOS, (b) Knight shift, and imaginary part of the transverse spin susceptibility as function of (c) temperature and (d) excitation energy with $T = 0$. All quantities are normalized to the normal-conducting bulk.

for $\epsilon \ll \Delta$ as shown in Fig. 2(a). The different surface states can be clearly distinguished by their decay lengths and energy dependencies. Furthermore, the MZMs oscillate with a period $v_{F,z}$ which is on the nm scale.

In figure 2(b) we plot the real part of the integrated local spin susceptibility which is proportional to the Knight shift $K(z) \sim \text{Re} \int dz' \chi_{zz}(z, z'; \mathbf{q}_{\parallel} = 0)$. Here, the distinction between the bulk and the surface is even clearer than for the LDOS. Because of the unequal-spin pairing, we find a significantly reduced contribution in the bulk for $T < \Delta$. However, $K(T \rightarrow 0)$ does not vanish because of the strong spin-orbit coupling [27]. In contrast, we find a large shift for $T \ll \Delta$ near the surface which is even larger than the bulk shift in the normal state because of the large midgap LDOS Eq. (6). The temperature dependence of the Knight shift is shown in Fig. 3(a) where the light feature is determined by the bulk and the weaker lines at larger K by the surface states. The Knight shift from the surface states is spread over a wide range due to the exponential decrease in the LDOS and shows peak-like subfeatures determined by the LDOS oscillations. The lines with largest shift originate from the surface where Dirac and MZMs sum up which gives rise to a very large LDOS and therefore a large spin response.

The imaginary part of the transverse spin susceptibility Fig. 2(c) is proportional to the NMR rate $1/(T_1 T) \sim \text{Im} \sum_{\mathbf{q}} \chi_{-+}(z, z; \mathbf{q}_{\parallel})$ [28]. Similarly to the Knight shift, we clearly distinguish between the bulk and the surface. The bulk states give rise to an activation law for $T \ll \Delta$ and the Hebel-Slichter coherence peak for $T \rightarrow \Delta$. In contrast, we find a finite $T = 0$ -value for $1/(T_1 T)$ near the surface where the contributions from the Dirac and the Majorana-like SABSs can be distinguished by their temperature behavior due to the almost constant LDOS of the Dirac modes. This temperature dependence

is shown in Fig. 3(b) where the surface contribution is again spread with peak-like subfeatures. However, the rate directly from the surface ($z \lesssim \xi_0$) is much larger than the rate from the MZM only ($z \gg \xi_0$) which allows to clearly distinguish the MZM from the Dirac modes.

In figure 2(d) we show the imaginary part of the dynamical transverse spin susceptibility as function of excitation energy. The spin excitation spectrum shows a very different behavior at the surface and in the bulk. For $\omega > 2\Delta E_0(k_F)/\mu$, there is a continuum of bulk spin excitations which is sharply bounded from below. In contrast, we find edge-edge spin excitations for $\omega < 2\Delta E_0(k_F)/\mu$ at the surface and bulk-edge spin excitations for $\omega > \Delta E_0(k_F)/\mu$. However, the intensity of the edge-edge spin excitations is significantly reduced as compared to the bulk-edge spin excitations.

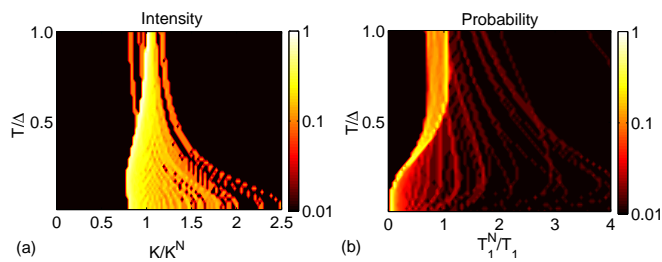


FIG. 3. (Color online) Distribution of (a) Knight shift and (b) spin-lattice relaxation rate as function of temperature. The bright features are determined by the bulk, while the broad subfeatures are the surface-state response. All quantities are normalized to the normal conducting bulk.

Finally, we discuss experimental measurement schemes of the spin susceptibility. In Refs. [29–31] it has been shown that ^{77}Se and ^{209}Bi NMR are suitable methods to investigate the bulk of Bi_2Se_3 where the dipole hyperfine coupling dominates due to the p -orbital character of the Fermi surface. We conclude that for low temperatures, NMR can also study the SC phase to determine the pairing symmetry. In our analysis, we find significant differences in the bulk spin response for the competing pairing symmetries [25]. The pairing Δ_2 yields a temperature independent Knight shift and a NMR rate with power-law T^5 , while Δ_3 shows a broadened Hebel-Slichter peak and an enhanced Knight shift because of a strongly momentum dependent gap. Hence, bulk NMR can clearly distinguish Δ_2 and Δ_3 from Δ , while Δ and Δ_1 are qualitatively similar. The response for Δ_1 is isotropic, whereas the Δ -case yields an anisotropic Knight shift [36]. As shown in Fig. 3, a more direct way to distinguish Δ and Δ_1 are the SABS for Δ which can be observed in powder samples and thin films as additional signals. The integrated intensity of the surface signal is reduced by a factor of ξ_1/L compared to the bulk signal where L is the thickness of the flakes. However, the surface signal shows a characteristic temperature behavior with decreasing spin susceptibility for $T \rightarrow \Delta$.

As shown in Fig. 2(c), the SABS yield a spatially dependent relaxation rate up to $v_z/\Delta \sim 200$ nm into the sample which is a characteristic signature for the topologically non-trivial nature of the SC state [25]. To investigate this local magnetism, depth resolved techniques such as μSR [18] and $\beta\text{-NMR}$ [19, 32] are suitable. In particular, they could differentiate the regimes with one, two, or three zero-energy SABS, which occur depending on the relative strength of the linear and quadratic terms in the Hamiltonian as discussed above. For Bi_2Se_3 , it has been shown that the implanted muons most probably stop in the van der Waals gap between quintuple layers [33]. Despite our concentration on NMR and μSR , our results are more general and can also be applied to ESR and surface sensitive spin-flip Raman scattering [34, 35].

Doped TIs usually have SC shielding fractions of 50% [12] while the rest is normal conducting. Here, bulk NMR could detect the mechanisms which determine this fraction. Depending on μ in the normal part of the sample, there might be additional signals which can be clearly distinguished from the SC ones by the very different temperature behavior. This key information about the distribution of dopants is an important step towards the understanding of unconventional SC in TIs. In this paper, we did not take vortices into account which can be distinguished from the SABS by their temperature behavior and the different length scales.

In conclusion, we have proposed a NMR experiment to determine the pairing symmetry of doped three-dimensional TIs and to observe the MZMs in the odd-parity interorbital unequal-spin pairing channel. Quadratic momentum terms significantly determine the character of the different species of unconventional SABSs. We have shown that the surface states of these systems have two characteristic length scales originating from the band inversion and the odd-parity pairing, and typically differ by two orders of magnitude. They contribute to a local spin susceptibility which can be clearly distinguished from the bulk by their characteristic temperature behavior and the large local density of states. Furthermore, we emphasize the usefulness of depth controlled local probes which directly show the existence of unconventional SABSs.

We acknowledge N. Georgieva, J. Haase, and D. Rybicki for useful discussions, and BMBF for financial support.

-
- [1] M. Z. Hasan, C. L. Kane, Rev. Mod. Phys. **82**, 3045 (2010).
 - [2] X.-L. Qi, S.-C. Zhang, Rev. Mod. Phys. **83**, 1057 (2011).
 - [3] A. P. Schnyder, S. Ryu, A. Furusaki, and A. W. W. Ludwig, Phys. Rev. B **78**, 195125 (2008).
 - [4] X. L. Qi, T. L. Hughes, S. Raghu, and S.-C. Zhang, Phys. Rev. Lett. **102**, 187001 (2009).

- [5] J. Linder, Y. Tanaka, T. Yokoyama, A. Sudbø, and N. Nagaosa, *Phys. Rev. Lett.* **104**, 067001 (2010).
- [6] M. Sato, *Phys. Rev. B* **81**, 220504(R) (2010).
- [7] H. Zhang, C. X. Liu, X. L. Qi, X. Dai, Z. Fang, and S.-C. Zhang, *Nat. Phys.* **5**, 438 (2009).
- [8] Y. S. Hor, A. J. Williams, J. G. Checkelsky, P. Roushan, J. Seo, Q. Xu, H. W. Zandbergen, A. Yazdani, N. P. Ong, and R. J. Cava, *Phys. Rev. Lett.* **104**, 057001 (2010).
- [9] L. A. Wray, S.-Y. Xu, Y. Xia, Y. S. Hor, D. Qian, A. V. Fedorov, H. Lin, A. Bansil, R. J. Cava, and M. Z. Hasan, *Nat. Phys.* **6**, 855 (2010); *Phys. Rev. B*, **83**, 224516 (2011).
- [10] P. Das, Y. Suzuki, M. Tachiki, and K. Kadowaki, *Phys. Rev. B* **83**, 220513(R) (2011).
- [11] M. Kriener, K. Segawa, Z. Ren, S. Sasaki, and Y. Ando, *Phys. Rev. Lett.* **106**, 127004 (2011); M. Kriener, K. Segawa, Z. Ren, S. Sasaki, S. Wada, S. Kuwabata, and Y. Ando, *Phys. Rev. B* **84**, 054513 (2011).
- [12] S. Sasaki, M. Kriener, K. Segawa, K. Yada, Y. Tanaka, M. Sato, and Y. Ando, *Phys. Rev. Lett.* **107**, 217001 (2011).
- [13] T. Kirzhner, E. Lahoud, K. B. Chaska, Z. Salman, and A. Kanigel, *Phys. Rev. B* **86**, 064517 (2012).
- [14] L. Fu, E. Berg, *Phys. Rev. Lett.* **105**, 097001 (2010).
- [15] L. Hao, T. K. Lee, *Phys. Rev. B* **83**, 134516 (2011).
- [16] A. Yamakage, K. Yada, M. Sato, and Y. Tanaka, *Phys. Rev. B* **85**, 180509(R) (2012).
- [17] T. H. Hsieh, L. Fu, *Phys. Rev. Lett.* **108**, 107005 (2012).
- [18] E. Morenzoni, F. Kottmann, D. Maden, B. Matthias, M. Meyberg, Th. Prokscha, Th. Wutzke, and U. Zimmermann, *Phys. Rev. Lett.* **72**, 2793 (1994).
- [19] G. D. Morris, W. A. MacFarlane, K. H. Chow, Z. Salman, D. J. Arseneau, S. Daviel, A. Hatakeyama, S. R. Kreitzman, C. D. P. Levy, R. Poutissou, R. H. Heffner, J. E. Elenewski, L. H. Greene, and R. F. Kiefl, *Phys. Rev. Lett.* **93**, 157601 (2004).
- [20] H. Lin, R. S. Markiewicz, L. A. Wray, L. Fu, M. Z. Hasan, and A. Bansil, *Phys. Rev. Lett.* **105**, 036404 (2010).
- [21] T. H. Hsieh, H. Lin, J. Liu, W. Duan, A. Bansil, and L. Fu, *Nat. Commun.* **3**, 982 (2012).
- [22] S. Sasaki, Z. Ren, A. A. Taskin, K. Segawa, L. Fu, and Y. Ando, arXiv:1208.0059.
- [23] S. B. Chung, S.-C. Zhang, *Phys. Rev. Lett.* **103**, 235301 (2009).
- [24] Y. Nagato, S. Higashitani, and K. Nagai, *J. Phys. Soc. Jpn.* **78**, 123603 (2009).
- [25] See supplemental materials for details.
- [26] N. Read, D. Green, *Phys. Rev. B* **61**, 10267 (2000).
- [27] P. W. Anderson, *Phys. Rev. Lett.* **3**, 325 (1959).
- [28] L. C. Hebel and C. P. Slichter, *Phys. Rev.* **113**, 1504 (1959).
- [29] D. Rybicki, N. Georgieva, and J. Haase (unpublished).
- [30] R. E. Taylor, B. Leung, M. P. Lake, and L.-S. Bouchard, *J. Phys. Chem. C* **116**, 17300 (2012).
- [31] B.-L. Young, Z.-Y. Lai, Z. Xu, A. Yang, G. D. Gu, Z.-H. Pan, T. Valla, G. J. Shu, R. Sankar, and F. C. Chou, *Phys. Rev. B* **86**, 075137 (2012).
- [32] M. M. Vazifeh, M. Franz, *Phys. Rev. B* **86**, 045451 (2012).
- [33] Z. Salman, E. Pomjakushina, V. Pomjakushin, A. Kanigel, K. Chashka, K. Conder, E. Morenzoni, T. Prokscha, K. Sedlak, and A. Suter, arXiv:1203.4850.
- [34] F. Perez, C. Aku-leh, D. Richards, B. Jusserand, L. C. Smith, D. Wolverson, and G. Karczewski, *Phys. Rev. Lett.* **99**, 026403 (2007).
- [35] L. Hao, P. Thalmeier, and T. K. Lee, *Phys. Rev. B* **84**, 235303 (2011).
- [36] T. Hashimoto, K. Yada, A. Yamakage, M. Sato, and Y. Tanaka, arXiv:1209.0656.

SUPPLEMENTARY MATERIAL FOR
“SURFACE STATES AND LOCAL SPIN SUSCEPTIBILITY IN DOPED THREE-DIMENSIONAL
TOPOLOGICAL INSULATORS WITH ODD-PARITY SUPERCONDUCTING PAIRING SYMMETRY”

Complementary to the main part of this paper, we here investigate the excitation spectra and the spin response of doped TIs with unequal-spin pairing and show that they are very different from the odd-parity interorbital case. We consider the (i) even-parity, intraorbital $\Delta_1(c_{1\uparrow}c_{1\downarrow} + c_{2\uparrow}c_{2\downarrow})$, (ii) odd-parity, intraorbital $\Delta_2(c_{1\uparrow}c_{1\downarrow} - c_{2\uparrow}c_{2\downarrow})$, and (iii) even-parity, interorbital $\Delta_3(c_{1\uparrow}c_{2\downarrow} - c_{1\downarrow}c_{2\uparrow})$ pairing symmetries.

As in the main part, we study the effect of spin-orbit coupling on the pairing symmetry by projecting the pairing terms onto the conduction band of the doped bulk TI. The conduction band is described by the operators $\alpha_{\mathbf{k},\tau} = \sum_{s,\sigma} \psi_{\tau}^{s,\sigma}(\mathbf{k}) c_{\sigma,\mathbf{k},s}$ with

$$\psi_{\tau}(\mathbf{k}) = \frac{1}{2\sqrt{E}} \begin{pmatrix} \sqrt{E + vk_{\tau}} e^{-i\chi/2} \\ \sqrt{E - vk_{\tau}} e^{i\chi/2} \end{pmatrix}_{\sigma} \otimes \begin{pmatrix} e^{-i(\phi/2 + \tau\pi/4)} \\ e^{i(\phi/2 + \tau\pi/4)} \end{pmatrix}_s \quad (7)$$

and $e^{i\chi} = (m_0(\mathbf{k}) + iv_z k_z) / \sqrt{m_0^2(\mathbf{k}) + v_z^2 k_z^2}$. The operators $\alpha_{\mathbf{k},\tau}$ satisfy the condition $\alpha_{(k,\phi+2\pi,k_z),\tau} = -\alpha_{(k,\phi,k_z),\tau}$, i.e. the operators are 4π periodic under rotation in momentum space. Because of the helical band structure, the operators $\alpha_{(k,\phi,k_z),\tau}$ transform into $\alpha_{(k,\phi+\pi,-k_z),\tau}$ under time reversal. Moreover, under parity transformation $\alpha_{(k,\phi,k_z),\tau}$ transforms into $\tau\alpha_{(k,\phi+\pi,-k_z),-\tau}$. Hence, it is straight forward to verify

the effective pairing

$$H_1 \approx \Delta_1 \sum_{\mathbf{k}, \tau} \alpha_{(k, \phi, k_z), \tau} \alpha_{(k, \phi + \pi, k_z), \tau} + h.c., \quad (8)$$

$$H_2 \approx \Delta_2 \sum_{\mathbf{k}, \tau} \frac{\tau v k}{\mu} \alpha_{(k, \phi, k_z), \tau} \alpha_{(k, \phi + \pi, k_z), \tau} + h.c., \quad (9)$$

$$H_3 \approx \Delta_3 \sum_{\mathbf{k}, \tau} \frac{m_0(\mathbf{k})}{\mu} \alpha_{(k, \phi, k_z), \tau} \alpha_{(k, \phi + \pi, k_z), \tau} + h.c.. \quad (10)$$

These equal pseudospin pairing terms do not vanish because of the 4π periodicity of the operators $\alpha_{(k, \phi, k_z), \tau}$. Even if these effective pairing symmetries are very similar, we observe differences in the effect on the Dirac surface states and characteristic bulk behavior when the mass term $m_0(\mathbf{k})$ changes sign. In figure 4, we plot the energy of the lowest quasiparticle level for the SC confined in z -direction as function of in-plane momentum k and chemical potential μ .

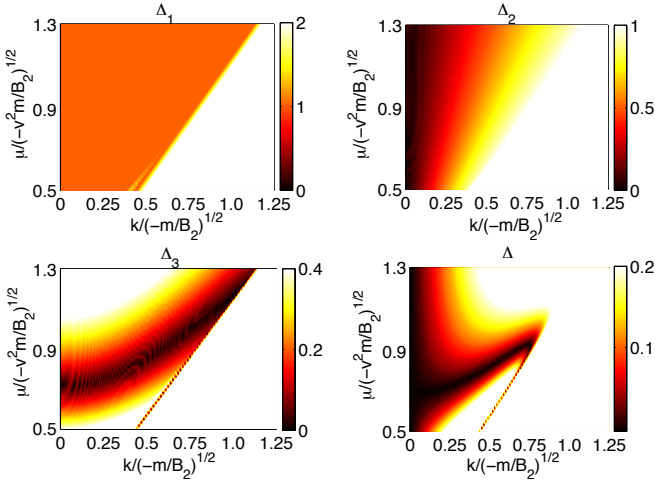


FIG. 4. (Color online) Lowest quasiparticle energy in units of Δ_i for the doped TI confined in z -direction and with (a) Δ_1 , (b) Δ_2 , (c) Δ_3 , and (d) Δ pairing as function of in-plane momentum k and chemical potential μ . Note the different color scales.

Even-parity intraorbital pairing Δ_1

For Δ_1 , the effective pairing Eq. (8) is intraband with the same amplitude for both pseudospins. Hence, we find conventional s -wave behavior for a metal with spin-orbit coupling. As shown in figure 4(a), the single-particle excitation spectra in the bulk and at the surface are both fully gapped with gap $2\Delta_1$. The gap at the surface originates from the fact that the helical Dirac modes have only contributions from one orbital and the pairing is intraorbital. We find that even if the Dirac modes are gapped, they do not hybridize with the bulk states because there is no particle-hole mixing between the bulk

and the surface and the gap at the surface arises from the pairing between the helical Dirac modes only.

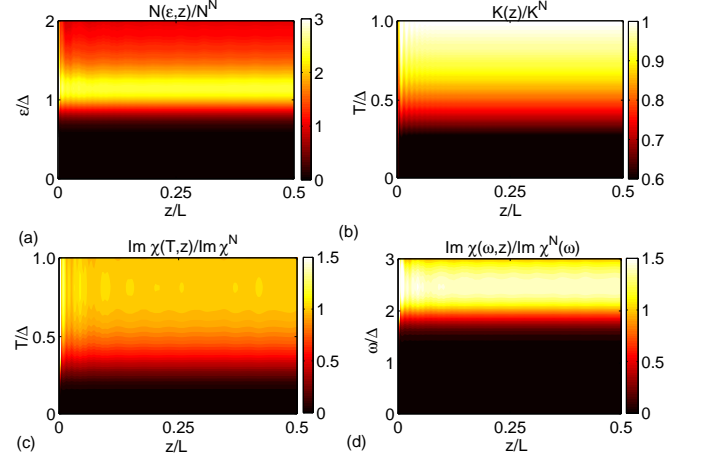


FIG. 5. (Color online) Δ_1 -pairing: (a) LDOS, (b) Knight shift, and imaginary part of the transverse spin susceptibility as function of (c) temperature and (d) excitation energy. All plots are normalized to the normal conducting bulk.

The LDOS is shown in Fig. 5(a) with an ordinary s -wave $\mathcal{N}_B(\epsilon) = 2\mu E_0(k_F)\epsilon/(\pi v^2 v_z \sqrt{\epsilon^2 - \Delta_1^2})$ in the bulk. Depending on whether the Dirac surface states of the TI already crossed the bulk states, we distinguish between $\mu^2 > v^2|m|/B_2$ with bulk contributions only and $\mu^2 < v^2|m|/B_2$ where

$$\mathcal{N}_S(\epsilon, z > 0) \approx \frac{\mu e^{-2z/\xi_0}}{\pi \xi_0 v^2} \frac{\epsilon}{\sqrt{\epsilon^2 - \Delta_1^2}}. \quad (11)$$

In our numerics, we only consider the case $\mu^2 > v^2|m|/B_2$ with Dirac modes.

As shown in Fig. 5(b), the Knight shift is significantly reduced in the bulk for $T < \Delta_1$ due to the SC gap and has a finite $T = 0$ value determined by the strong spin-orbit coupling. The temperature dependence of the Knight shift distribution is plotted in Fig. 6(a) where the dark feature is the signal from the bulk with a characteristic decrease for $T \rightarrow 0$. The line with larger shift originates from the Dirac surface states and shows qualitatively the same temperature dependence as the bulk shift as expected from the gapped LDOS.

Similarly to the Knight shift, we find conventional s -wave behavior for $1/(T_1 T)$ in the bulk and at the surface with an activation law for $T \ll \Delta_1$ and the Hebel-Slichter coherence peak for $T \rightarrow \Delta_1$ as shown in Fig. 5(c) and Fig. 6(b). Again, the surface shows qualitatively the same behavior as the bulk but with a much larger rate due to the large surface LDOS. The transition between the characteristic surface and bulk behaviors occurs in a depth ξ_0 .

In figure 5(d) we plot the imaginary part of the transverse spin susceptibility as function of excitation energy.

For $\omega > 2\Delta_1$, there is a featureless continuum of bulk spin excitations which is sharply bounded from below at $\omega = 2\Delta_1$ because of the quasiparticle gap. Again we find a larger spin susceptibility at the surface as compared to the bulk as a consequence of the large LDOS from the Dirac modes.

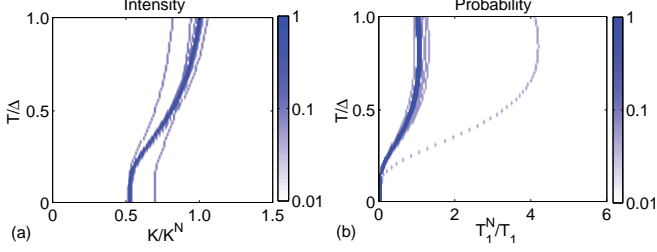


FIG. 6. (Color online) Δ_1 -pairing: Distribution of the temperature dependent (a) Knight shift and (b) NMR rate. All plots are normalized to the normal conducting bulk. The dark features are determined by the bulk, while the subfeatures show the Dirac surface response.

Odd-parity intraorbital pairing Δ_2

For Δ_2 -pairing, the orbitals pair into singlets with a relative minus sign. Because of this relative minus sign, the effective pairing term Eq. (9) is linear in k and vanishes for $k_x = k_y = 0$ which gives rise to point nodes in the bulk single-particle excitation spectrum and a linear dispersion for $\epsilon \ll \Delta_2$. However, for the Dirac modes with $\mu = vk$, we find as for the even parity case a gap $2\Delta_2$.

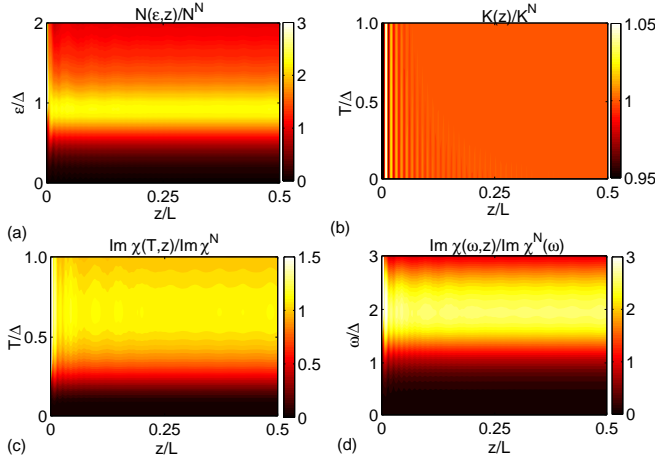


FIG. 7. (Color online) Δ_2 -pairing: (a) LDOS, (b) Knight shift, and imaginary part of the transverse spin susceptibility as function of (c) temperature and (d) excitation energy. All plots are normalized to the normal conducting bulk.

In figure 7(a) we plot the LDOS for Δ_2 -pairing which is finite for all $\epsilon > 0$ due to the linear dispersion and

shows a cusp at $\epsilon = \Delta_2$. In the bulk, we find for the LDOS the conventional result for SCs with point nodes,

$$\mathcal{N}_B(\epsilon) = 2 \frac{\epsilon \mu E_0(k_F)}{\Delta_2 \pi v^2 v_z} \log \left| \frac{\epsilon + \Delta_2}{\epsilon - \Delta_2} \right|. \quad (12)$$

As before, we distinguish between $\mu^2 > v^2|m|/B_2$ with bulk contributions only and $\mu^2 < v^2|m|/B_2$ with

$$\mathcal{N}_S(\epsilon, z > 0) \approx \frac{\mu e^{-2z/\xi_0}}{\pi \xi_0 v^2} \frac{\epsilon}{\sqrt{\epsilon^2 - \Delta_2^2}}. \quad (13)$$

The different energy dependence of the bulk and the surface dispersion yields strong evidence for different characteristic temperature behavior in the bulk and at the surface.

As shown in Figs. 7(b) and 8(a), the Knight shift is essentially independent of temperature even for $T < \Delta_2$. Here, the weak subfeatures at smaller shift originate from the Dirac surface states and show an s -wave behavior with reduced Knight shift below T_c in contrast to the constant bulk value.

In figure 7(c) we plot the NMR rate which is much larger at the surface than in the bulk. The temperature dependence of the rate is shown in Fig. 8(b) where we can clearly distinguish between bulk and surface contributions. In stark contrast to the constant Knight shift, we find for $T \rightarrow 0$ a power law T^5 in the bulk which is characteristic for point nodes and an activation law $\exp(-\Delta_2/T)$ from the surface contribution. For $T \rightarrow \Delta_2$ we obtain a Hebel-Slichter peak at the surface whereas the bulk yields just a small coherence peak due to the broadened LDOS Eq. (12).

The imaginary part of the dynamical transverse spin susceptibility is shown in Fig. 7(d) as function of the excitation energy. For all ϵ there is a continuum of single-particle spin excitations with an amplitude that behaves as function of energy like $\mathcal{N}_B^2(\omega/2, z)$ in the bulk and like $(\mathcal{N}_B(\omega/2, z) + \mathcal{N}_S(\omega/2, z))^2$ at the surface. For $\omega \approx 2\Delta_2$, there is a peak in the spin spectrum resulting from the cusp in the LDOS.

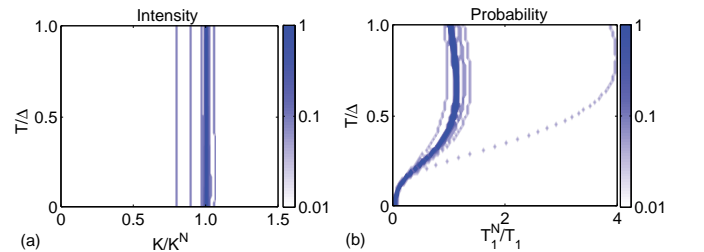


FIG. 8. (Color online) Δ_2 -pairing: Distribution of the temperature dependent (a) Knight shift and (b) NMR rate. All plots are normalized to the normal conducting bulk. The dark feature is determined by the bulk, while the subfeatures show the Dirac surface response.

Even-parity interorbital pairing Δ_3

The effective pairing Hamiltonian for Δ_3 is shown in Eq. (10) with a fully gapped bulk single-particle excitation spectrum for $m_0(\mathbf{k}_F) \neq 0$ and a momentum dependent gap $2\Delta_3|m_0(k)|/\mu$. Since $m_0(k)$ changes sign when k increases because of the band inversion at $k = 0$, we find a gap closing and reopening as function of μ which is intricately related to the transition from the TI phase into the band insulator phase. Furthermore, Δ_3 does not gap the Dirac modes for which $m_0(k, -i\nu/v_z) = \nu$ and the contributions from ν and $-\nu$ cancel. However, from the quasiparticle energies we see that the bulk spectrum shows nodes whenever $m_0(k)$ changes sign as shown in Fig. 4(c). Similarly to the Δ case, we here find three qualitatively distinct sectors with transitions at $\mu^2 = -mv_z^2/B_1$ and $\mu^2 = -mv^2/B_2$. The origin of the nodes and distinct sectors is again the band inversion near $k = 0$ which changes into the trivial band order along the gapless line in Fig. 4(c). However, in contrast to the odd-parity interorbital case, here, the gapless modes are bulk modes. In our numerics, we only consider the case $\mu^2 < -mv_z^2/B_1 < -mv^2/B_2$, where the bulk is fully gapped and the Dirac modes are ungapped.

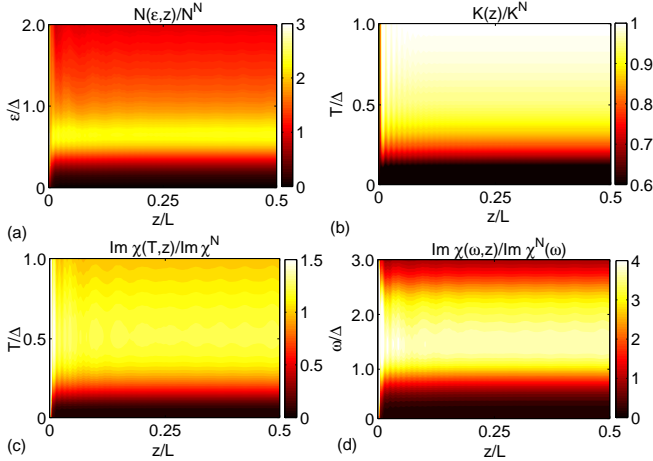


FIG. 9. (Color online) Δ_3 -pairing: (a) LDOS, (b) Knight shift, and imaginary part of the transverse spin susceptibility as function of (c) temperature and (d) excitation energy. All plots are normalized to the normal conducting bulk.

As shown in Fig. 9(a), the LDOS in the bulk $\mathcal{N}_B(\epsilon) = 2\mu E_0(k_F)\epsilon/(\pi v^2 v_z \sqrt{\epsilon^2 - \Delta_3^2 m_0^2(k_F)/\mu^2})$ with a quasi-particle gap $2\Delta_3|m_0(k_F)|/\mu$. From this expression, we see that the gap closes when $m_0(k)$ vanishes and decreases with increasing μ . As before, we distinguish between $\mu^2 > v^2|m|/B_2$ where only the bulk contributes and $\mu^2 < v^2|m|/B_2$ with a gapless surface LDOS

$$\mathcal{N}_S(\epsilon, z > 0) \approx \frac{\mu e^{-2z/\xi_0}}{\pi \xi_0 v^2}. \quad (14)$$

In figure 9(b) we plot the Knight shift $K(z)$ with qual-

itatively very different behavior in the bulk and at the surface. In the bulk we find a reduced shift for $T < \Delta_3$ with a finite $K(T \rightarrow 0)$ due to the strong spin-orbit coupling. In contrast, at the surface we find a larger shift for $T \ll \Delta_3$ because of the strongly spin-orbit coupled massless surface states. The temperature dependence of the Knight shift is shown in Fig. 10(a) where the strong feature is determined by the bulk and the second line by the Dirac modes.

In figure 9(c) we find similarly to the Knight shift a qualitatively different behavior for the NMR rate in the bulk and at the surface. The gapped bulk gives rise to an activation law for $T \ll \Delta_3$ and a Hebel-Slichter coherence peak for $T \rightarrow \Delta_3$. In contrast, we find a finite $T = 0$ -value for $1/(T_1 T)$ at the surface which is characteristic for metallic states. The temperature dependence is also plotted in Fig. 10(b) where the rate from the Dirac states is much larger than the rate from the bulk because of the large gapless LDOS.

In figure 9(d) we show the imaginary part of the dynamical transverse spin susceptibility as function of excitation energy. The excitation spectrum shows a very different behavior at the surface and in the bulk. For $\omega > 2\Delta_3|m_0(k_F)|/\mu$, there is a continuum of excitations in the bulk which is sharply bounded at $\omega = 2\Delta_3|m_0(k_F)|/\mu$. In addition, we find low-energy spin excitations at the surface and bulk-edge excitations for $\omega > \Delta_3|m_0(k_F)|/\mu$ within a length ξ_0 into the sample.

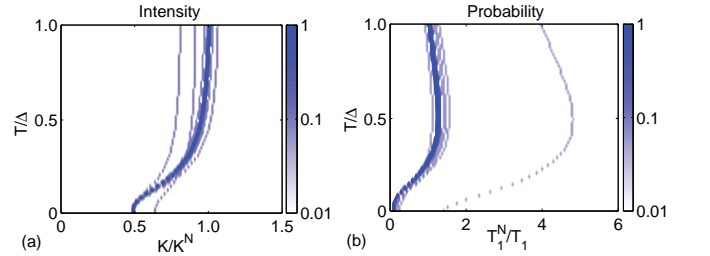


FIG. 10. (Color online) Δ_3 -pairing: Distribution of the temperature dependent (a) Knight shift and (b) NMR rate. All plots are normalized to the normal conducting bulk. The dark features are determined by the bulk, while the subfeatures show the Dirac surface response.

Odd-parity interorbital pairing Δ

In the main part of this paper we showed that for $\mu > |m| \gg \Delta$ the odd-parity interorbital pairing Hamiltonian can be mapped onto a time-reversal invariant $p \pm ip$ pairing. Furthermore, we found that this pairing symmetry gives rise to a Kramers pair of MZMs at the time-reversal invariant momentum $k = 0$ and a pair of zero-energy SABs whenever $m_0(\mathbf{k}_F) = 0$. In contrast, the bulk single-particle excitation spectrum is always fully gapped with weakly momentum dependent

gap $\Delta\sqrt{1 - m_0^2(\mathbf{k}_F)/\mu^2} > 0$. The aim of this section is to get insight into the quasiparticle spectrum for different parameter regimes.

At the surface we find an interesting spectrum as shown in Fig. 4(d) where we see a pair of $k = 0$ MZMs for all μ and depending on the chemical potential, we find three regimes which can be distinguished by the number of additional finite- \mathbf{k} zero-energy modes. However, in contrast to the $k = 0$ mode, the finite- \mathbf{k} modes are not MZMs in the sense that they are equal superpositions of electron and hole creation operators such that $\gamma = \gamma^\dagger$. Instead, the Bogoliubov operators for these finite- \mathbf{k} modes satisfy $\gamma_{\mathbf{k}} = \gamma_{-\mathbf{k}}^\dagger$ with a finite electron-hole imbalance. For $\mu^2 < -mv_z^2/B_1$, we find additionally to the $k = 0$ MZM one pair of finite \mathbf{k} zero-energy modes located at $k = \mu/v$ originating from the band inversion of the TI. They are protected by the mirror helicity of the Hamiltonian and henceforth not gapped as can be seen from the effective pairing Eq. (3). In the following, we consider the two cases $-mv_z^2/B_1 \gtrless -mv^2/B_2$ which are shown in Fig. 11. When tuning through the point $\mu^2 = -mv_z^2/B_1 < -mv^2/B_2$, the sign of the mass term $m_0(k_{F,z})$ changes which gives rise to another finite- \mathbf{k} zero-energy mode which carries the negative sign originating from the band inversion. This additional mode is shown as the dark dispersing feature in Fig. 4(d). The momentum of the third mode increases with increasing chemical potential like

$$k \approx \sqrt{\frac{B_1\mu^2 - |m|v_z^2}{B_1v^2 - B_2v_z^2}} \quad (15)$$

and for $\mu^2 = -mv^2/B_2$ the finite- \mathbf{k} zero-energy modes fuse and gap out due to the vanishing of the band inversion. Hence, we find only the $k = 0$ MZMs for $\mu^2 > -mv^2/B_2 > -mv_z^2/B_1$. For $-mv_z^2/B_1 \gg -mv^2/B_2$, we find a different behavior because the Dirac modes enter the bulk for $\mu^2 \rightarrow -mv_z^2/B_2$. Thus, the finite k zero mode loses its Dirac character and moves towards zero momentum as described by Eq. (15). However, this mode is still protected by the mirror helicity and can only disappear for $\mu^2 \rightarrow -mv_z^2/B_1$. Thus, the phase with three zero-energy modes is absent in this case as shown in Fig. 11(a). For $-mv_z^2/B_1 \gtrless -mv^2/B_2$, both processes compete. In figure 11(b), we show that in this case another finite k zero energy mode emerges while the Dirac-like zero-energy mode moves towards zero momentum. When the finite k zero-energy modes cross, they gap out. All these findings are in excellent agreement with our projection analysis in the main part of this paper.

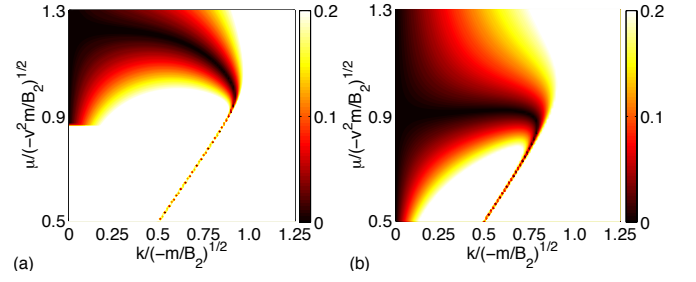


FIG. 11. (Color online) Lowest quasiparticle energy in units of Δ with $v = 4 \text{ eV \AA}$ and $m = -0.3 \text{ eV}$. (a) Regime with $v^2/B_2 < v_z^2/B_1$ and $v_z = 2 \text{ eV \AA}$, $B_1 = 5 \text{ eV \AA}^2$, $B_2 = 40 \text{ eV \AA}^2$; (b) Regime with $v^2/B_2 = v_z^2/B_1$ and $v_z = 4 \text{ eV \AA}$, $B_1 = B_2 = 10 \text{ eV \AA}^2$.

Knight shift and NMR rate in the bulk

In figure 12(a) and (b), we summarize and compare the results for the spin response of the bulk for the above introduced pairing symmetries. In this section we assume that the order parameter Δ_i is temperature dependent with $\Delta_i(T) = \Delta_i \sqrt{1 - T/1.76\Delta_i}$.

For the Knight shift Fig. 12(a), we find three different behaviors below T_c . All pairing terms yield a finite value for the zero-temperature spin susceptibility because of the strong spin-orbit coupling [27]. However, for Δ , Δ_1 , and Δ_3 we find a decrease of the Knight shift below T_c with a similar functional behavior for Δ_1 and Δ which differ by $K_N/4$ for $T = 0$. For Δ_3 we observe a qualitatively similar temperature dependence but the functional form is very different as for Δ and Δ_1 because of the strongly momentum dependent quasiparticle gap. In stark contrast to these reduced Knight shifts, we find no change of the Knight shift for Δ_2 below T_c . This also shows that a constant Knight shift for $T < T_c$ is not a clear signature for triplet pairing symmetry and can also appear for singlet pairing symmetries.

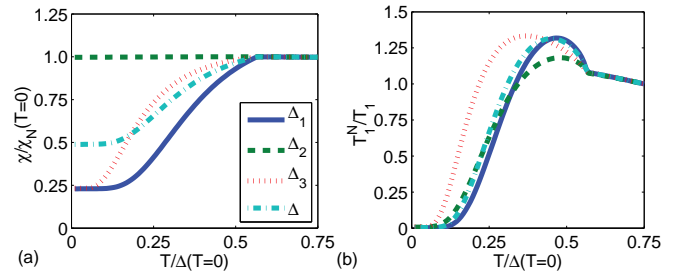


FIG. 12. (Color online) Temperature dependence of (a) the Knight shift and (b) the spin-lattice relaxation rate in the bulk for the different pairing symmetries with $\Delta_i = 1 \text{ meV}$. The lines are defined in panel (a).

In the NMR rate Fig. 12(b), the differences between the pairing symmetries are not as strong as for the Knight shift. For Δ and Δ_1 , we find conventional s -wave type

behavior with an activation law for $T \rightarrow 0$ and a sharp Hebel-Slichter coherence peak for $T \rightarrow T_c$. However, we can again clearly distinguish Δ_2 and Δ_3 from Δ and Δ_1 by their functional dependence. As shown above, we find a power-law T^5 behavior for Δ_2 due to the point nodes and for Δ_3 , the curve is compressed towards $T = 0$ due to the momentum-dependent gap and shows no sharp coherence peak.

Hence, we conclude that it is clearly possible in an

experiment to distinguish Δ and Δ_1 from other unequal-spin pairing symmetries by conventional bulk NMR experiments while for the distinction between Δ and Δ_1 quantitative comparisons are necessary. However, an even clearer distinction between Δ_1 and Δ can be obtained by probing the existence of SABs in powder samples or thin films, or even better depth controlled local probes such as μ SR and β -NMR.